EASR

Engineering and Applied Science Research

https://www.tci-thaijo.org/index.php/easr/index

Published by the Faculty of Engineering, Khon Kaen University, Thailand

Normal pressure effects upon mechanical properties and microstructure of Ti-6Al-4V and AA2024 rotary friction welds

Lakache Houssem Eddine*[1)], May Abdelghani[1)] and Badji Riad[2)]

[1)]Laboratoire Génie des Matériaux, École Militaire Polytechnique, Alger 16042, Algeria
[2)]Research Centre in Industrial Technologies (CRTI), Cheraga, Alger 16014, Algeria

Received 22 January 2023
Revised 13 March 2023
Accepted 22 March 2023

Abstract

The aim of this work is to investigate the effect of normal pressure upon the mechanical properties and their related microstructures of the similar Ti-6Al-4V and AA2024 Rotary Friction Welding (RFW) joints. The main characteristic of this process is the use of friction to generate adequate energy and raise temperature locally in order to create favorable conditions for welding at the interface between two parts. Successful welds were produced showing, among many others, that the fracture occurres at the weld interface for the AA2024 alloy, hence its low tensile strength. However, the fracture occurres outside the weld interface for the Ti-6Al-4V alloy, which indicates that the weld joint is more resistant than the base metal. The microscopic observation of the fracture surfaces of the AA2024 samples exhibits a mixture of morphologies with a majority of rough cupular surfaces, indicating a dominant ductile fracture mode. For the Ti-6Al-4V RFW joints, cupules of different sizes are observed over the entire surface that also exhibits a ductile fracture mode.

Keywords: Rotary Friction Welding (RFW), Fracture, Microstructure, Mechanical properties, AA2024, Ti-6Al-4V

1. Introduction

Following the guidelines of the American Welding Society C6.1-89 standard [1], Rotary Friction Welding (RFW) is an entirely solid-state technique that ensures the peak temperature remains below the melting points of the materials being welded. This process is primarily utilized for joining cylindrical rods and tubes that have relatively smaller dimensions [2]. The basic configuration of the RFW process equipment requires a rigid structure to ensure the stability of components operating at high speeds and driven by high-pressure forging. Works on the construction of RFW setups are rare, and the equipment used during these experiments has the same principle but with different designs.

The RFW process generates plastic deformation and heat input during the friction phase, while the forging phase triggers the interdiffusion phenomenon at the weld interface [3]. The demand for a welding process that can join materials like titanium, known for its high strength and good corrosive properties, and aluminum, renowned for its low cost and lightness, has resulted in numerous experimental studies conducted by researchers worldwide [4]. Avinash et al. [5] have investigated the mechanical behavior and microstructure of similar Ti-6Al-4V RFW joints, achieving high microhardness and tensile strength using a rotational speed of 1500 rpm. Similarly, Nu et al. [6] studied the influence of RFW parameters on Ti-6Al-4V weld joints, finding that optimal parameters included a rotational speed of 1200 rpm, friction time of 4 s, forging time of 2 s, and normal pressure of 40 MPa. Several other works have also focused on investigating the mechanical properties and microstructure of similar titanium alloys RFW joints [7-11]. Furthermore, Hynes and Velu [12] experimentally investigated the effect of rotational speed on the bonding process at the interface of dissimilar Ti-6Al-4V/AA6061 RFW joints, finding that increased rotational speed led to dynamic recrystallization and the recovery of recrystallized grains, ultimately boosting joint strength.

Additionally, Li et al. [13, 14] conducted extensive research on the impact of inhomogeneous microstructure, mechanical properties, and corrosion behavior on AA2024 RFW joints to emphasize their relationship. In recent years, there has been growing interest in the mechanical behavior of aluminum alloys, particularly in their cyclic behavior. Prior research has investigated the mechanical behavior of AA2017 and AA2024 aluminum alloys, leading to the evaluation of their physical and mechanical characteristics. For instance, previous researchers have conducted several studies on the cyclic behavior of these alloys and their mechanical properties. These studies have shed light on the unique characteristics of these alloys and have helped to advance our understanding of their behavior under various conditions [15-21].

Recently, the research work done by Lakache et al. [22] aims to optimize the AA2024 RFW parameters based on experimental study of the weld joints. The best compromise that offers a tensile strength value of 499 MPa corresponds to the RFW joint obtained by using normal pressure of 12 MPa and rotational speed of 2000 rpm. Li et al. [23] employed RFW to join similar AA6061-T6 joints and examine the influence of rotational speed on friction behavior. Similarly, Hariprasath et al. [24] analyzed the metallurgical characteristics and mechanical properties of similar AA7075 RFW joints, reporting a maximum tensile strength of 472 MPa. Dang et al. [25] investigated the effects of RFW process parameters on intermetallic compound evolution and tensile strength of dissimilar

*Corresponding author.
Email address: lakache.houssem@gmail.com
doi: 10.14456/easr.2023.19

AA2219/304 stainless steel weld joints. They found that medium normal pressure (120 MPa) and moderate rotational speed (1100 rpm) produced high-quality weld joints, but high heat input led to severe degradation of mechanical properties. Dong et al. [26] investigated the inhomogeneous properties of dissimilar AA5052/304 stainless steel RFW joints. Additionally, authors have used Friction Stir Welding (FSW) to successfully join similar aluminum alloys like AA7039 [27], AA2024 [28, 29], and AA2017 [30].

This study used a recently implemented RFW device on a RAMO-T37 parallel lathe to create similar Ti-6Al-4V and AA2024 weld joints. The objective of this research was to identify the optimal normal pressures for achieving desirable mechanical properties and microstructural analysis.

2. Experimental study

Cylindrical rods measuring Ø 15 mm x 60 mm were prepared for welding. The material used (Ti-6Al-4V and AA2024) was analyzed for its chemical composition through Energy Dispersive X-ray (EDX) analyses, as shown in Table 1 and Figures 1(a)-(b).

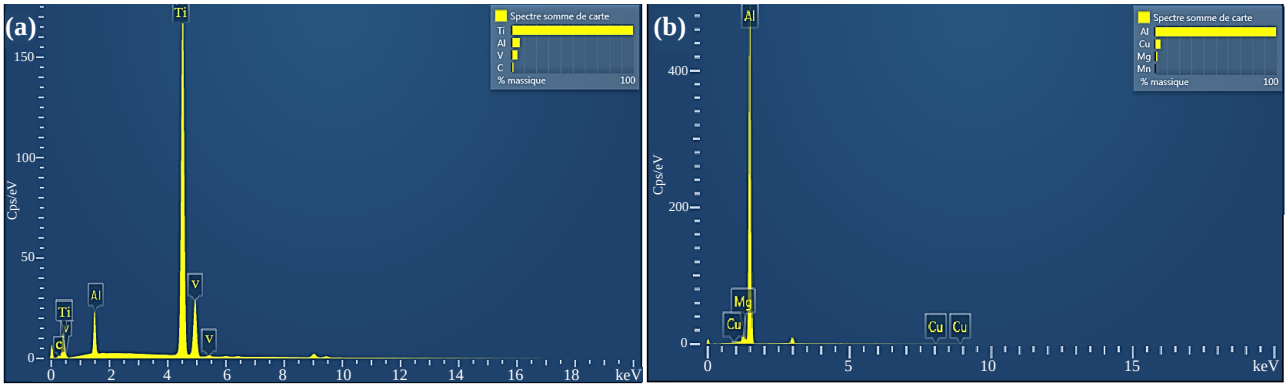

Figure 1 EDX spectrums for (a) Ti-6Al-4V, and (b) AA2024.

Table 1 Chemical composition of materials (weight %)

Elements	*Al*	*Cu*	*Mg*	*C*	*Ti*	*V*	*Mn*	*Fe*	*Si*
AA2024	92.5	3.9	1.2	-	-	-	0.7	0.5	0.6
Ti-6Al-4V	7.2	-	0.2	1.2	87 .2	4.3	-	-	-

To measure temperature, two k-type thermocouples were fixed onto relevant areas. One thermocouple was positioned at the center where the two parts were brought into contact, while the other was placed 5 mm away from the weld interface on the fixed side.

To analyze the mechanical properties of the welds, 6 mm nominal diameter samples were machined from the RFW joints in accordance with ISO 6892-1: 2016 (E)-Standard [31] and subjected to tensile tests at a strain rate of 10^{-3} s^{-1}. Prior to microscope examination, the AA2024 and TiAl6V4 samples underwent axial polishing and chemical etching with reagents (3ml HCl + 2ml HF + 20ml water) and (2ml HNO3 + 1ml HF+17ml water) respectively for 15 s. Vickers microhardness values were measured using a load of 500 g for the Ti-6Al-4V sample and 300 g for the AA2024 sample. The weld interface was traversed over a distance of ± 10 mm with a 1 mm step. Fracture surfaces were examined using TESCAN MIRA 3 Scanning Electron Microscopy operating in backscattered electron (BSE) emission mode after conducting the tensile tests.

The RFW process requires the application of pressure forces; for this, a double-acting hydraulic cylinder is used, as shown in Figure 2(a), connected to a hydraulic unit instrumented by a pressure sensor. An oil flow limiter is mounted on the hydraulic unit to control the advance speed of the cylinder piston. A pneumatic cylinder placed above the lathe brake to replace the human operator's foot action, as indicated in Figures 2(b)-(c) provides braking. The action of the brake is delivered via a pneumatic distributor that is supplied with a pressure of 0.6 MPa.

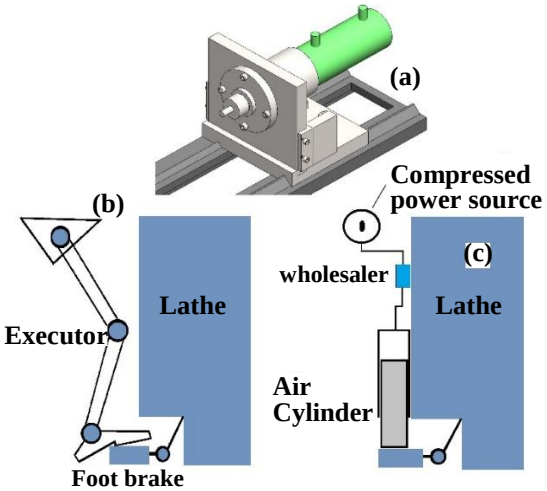

Figure 2 (a) Device designed for RFW process, (b) Braking by an operator, (c) Automatic braking by a pneumatic system.

The automated RFW setup's elements are driven by a computer program (Figure 3) that regulates the friction phase at pressure P1 for a specific time t1, followed by a braking-induced stop of rotation during the forging phase at pressure P2 for the corresponding time t2. Finally, the cylinder piston returns to eliminate the pressure applied on the weld joint. The RFW parameters are entered on a LabVIEW interface, which streamlines the process for users. The interface is composed of connection ports that define the acquisition card and control card, input boxes for the RFW parameters, a sensor for pressure variations, light indicators for each phase of the process, and START button to initiate the RFW process.

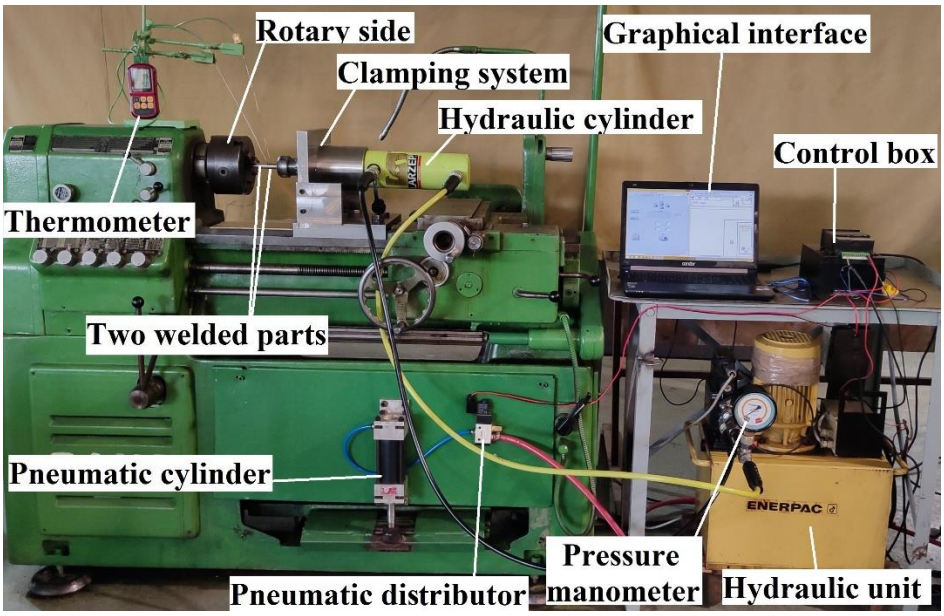

Figure 3 The automated RFW setup.

To manage the RFW process parameters and gather data, an HX711 module equipped with a 24-bit weighing pressure sensor is utilized to increase the voltage values collected by the pressure sensor. The control system includes two Arduino Uno boards; for data acquisition and executing commands, and a multi-channel relay module for linking the electronic components. Figure 4 displays the connections within the RFW control arrangement. Electrical energy pertains to peripherals directly connected to the power supply, such as the hydraulic pressure sensor, hydraulic distributor, and pneumatic distributor. This research necessitates the use of two Arduino compilers and LabVIEW software. The first compiler is employed solely for equipment testing and pressure acquisition, while the second one is utilized to program the RFW process and develop an interface that streamlines user operations.

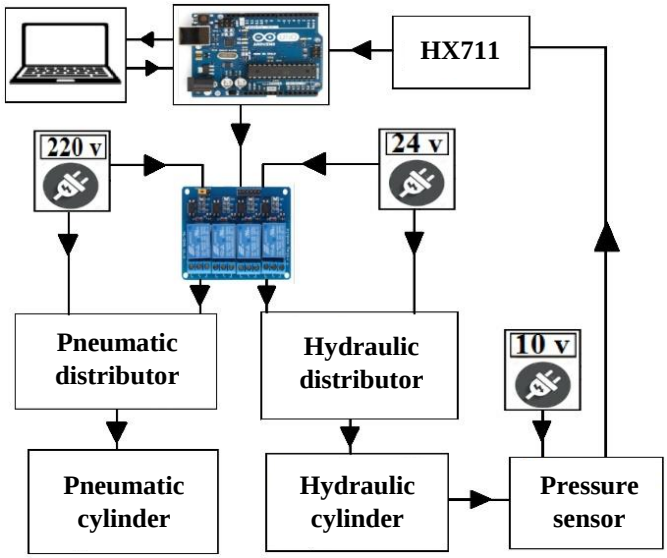

Figure 4 RFW control configuration.

3. Results

A set of procedures are followed during the RFW process to examine the impact of normal pressure on the outcome, as outlined in Table 2. The remaining parameters, including a rotational velocity of 2000 rpm for Ti-6Al-4V alloy and 1600 rpm for AA2024, a friction and forging time of 6 seconds each, are held constant. The similar Ti-6Al-4V and the AA2024 RFW joints are presented in Figure 5.

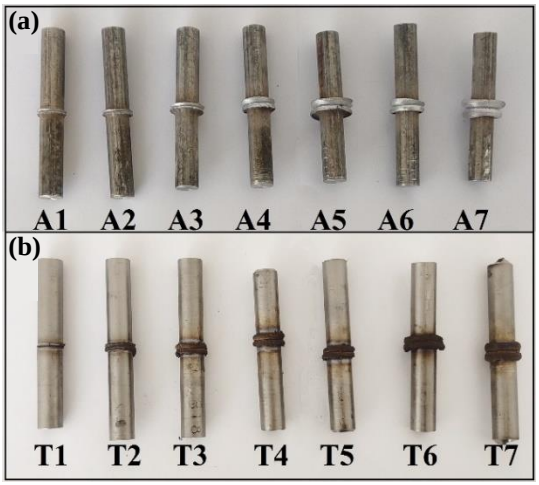

Figure 5 RFW joints for (a) AA2024, and (b) Ti-6Al-4V.

Table 2 Normal pressure values

AA2024 sample	***A1***	***A2***	***A3***	***A4***	***A5***	***A6***	***A7***
Normal pressure [MPa]	2	4	6	8	10	12	14
Ti-6Al-4V sample	***T1***	***T2***	***T3***	***T4***	***T5***	***T6***	***T7***
Normal pressure [MPa]	2	4	6	8	10	12	14

The first measurement point of the interfacial temperature (Pt 1) concerns the dynamically recrystallized zone (DRZ), and the second point (Pt 2) designates the heat affected zone (HAZ) (see Figure 6(a)). The interfacial temperature increases when the normal pressure rises because the friction forces are greater, which will generate more heat. This heat will be propagated by conduction in the metal along the longitudinal direction as shown in Figure 6(b). Besides, it will be propagated by convection in the air as illustrated in Figure 6(c).

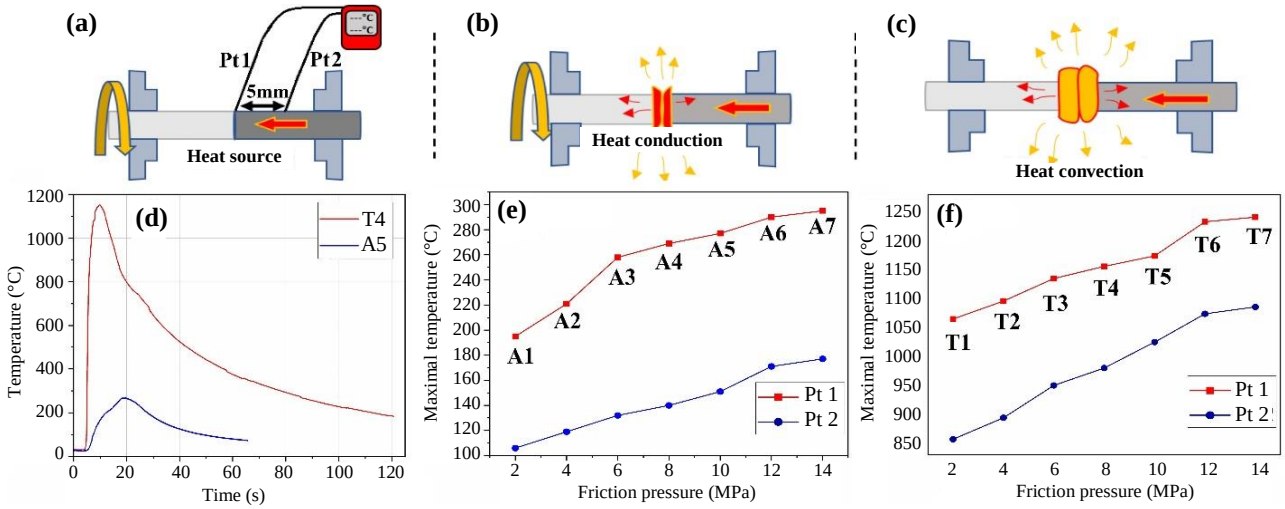

Figure 6 (a) Accosting phase, (b) Friction phase, (c) Forging phase, (d) Thermal cycles for A4 and T3 samples, (e and f) Normal pressure dependent maximal interfacial temperature for AA2024 and Ti-6Al-4V respectively.

Figures 6(e)-(f) show the maximum interfacial temperature in relation to normal pressure for the AA2024 and Ti-6Al-4V alloys. Even though the two measuring points are separated by a 5mm distance, there is an approximate temperature gradient of 200 °C between them for the Ti-6Al-4V alloy, with temperatures reaching as high as 1236 °C. Conversely, due to the high ductility of the aluminum alloy and its low melting point (658 °C), the temperature for the AA2024 alloy does not surpass 295 °C. The microstructure achieved through heat treatment is dependent on the dissolving field (α + β or β) and the cooling rate utilized [32, 33]. The evolution of the volume fraction of the phases varies according to the empirical formula (1) proposed by Castro and Seraphin [34].

$$\%\beta = 92.5 * e^{-0.0085*(980^{\circ}-T)} + 7.5 \quad (1)$$

As depicted in Figures 6(d) and 6(f), the T4 sample experiences temperatures of 1151 °C. The α phase is dissolved during the heating process, and the β phase fraction rises until it reaches 100% beyond the transition temperature Tβ (980 °C), leading to a microstructure composed solely of the β phase. Cooling the Ti-6Al-4V alloy from the β domain results in either an lamellar or acicular structure, with the lamellae thickness influenced by the cooling rate [35, 36]. The maximum temperature recorded for the AA2024 weld joints is 270 °C for A5, which affects both the microstructure and mechanical properties of the HAZ.

3.1 Mechanical behavior

The primary objective of the tensile test is twofold: to identify the fracture zone and evaluate the efficacy of the weld joint strength by utilizing Equation (2), as is done in this research [37, 38].

$$Eff(\%) = 100 * \left({Rm_{weld}}/{Rm_{BM}}\right) \quad (2)$$

Figures 7(a)-(b) and Table 3 provide a summary of the tensile test results. The fracture occurs in the center of the Ti-6Al-4V alloy and outside of the central zone with a 45° angle for the AA2024 alloy in the unwelded samples representing the base metal (BM). It is noteworthy that the fracture took place beyond the joint's interface in all Ti-6Al-4V RFW joints, indicating that the weld joint's strength surpasses that of the base metal. The curves are almost indistinguishable in appearance, with a slight variance in values, characterized by an elastic linear section and a plastic domain that is more apparent for the Ti-6Al-4V alloy. The fractured Ti-6Al-4V samples exhibit a significant necking of the section, while the AA2024 alloy shows no necking since the fracture usually happens in the center that is the weakest area that represents the zone of stress concentration. These results are consistent with the findings of Li et al. [14].

Table 3 Tensile tests results

	Sample	E (GPa)	Re0.2 (MPa)	Rm (MPa)	A (%)	Eff (%)	Fracture zone
AA2024	BM	77.64	395.85	486.34	13.36	-	On side
	A1	63.05	339.45	347.17	5.85	71.38	DRZ
	A2	73.78	301.44	414.26	6.94	85.18	DRZ
	A3	75.99	265.81	429.08	4.92	88.23	DRZ
	A4	68.58	314.23	454.90	10.15	93.54	TMAZ
	A5	68.23	294.52	460.09	7.75	94.60	TMAZ
	A6	67.38	309.04	434.92	10.04	89.43	DRZ
	A7	67.29	191.71	288.59	3.55	59.34	DRZ
Ti-6Al-4V	BM	107.29	946.88	991.89	15.31	-	In center
	T1	110.85	815.34	857.59	9.06	86.46	HAZ
	T2	108.01	854.61	915.81	9.27	92.33	HAZ
	T3	113.38	987.42	1017.75	10.26	102.61	HAZ
	T4	115.70	997.52	1031.23	10.96	103.97	HAZ
	T5	98.35	932.65	975.58	11.10	98.36	TMAZ
	T6	106.83	965.10	996.52	10.12	100.47	HAZ
	T7	104.09	939.91	972.36	10.68	98.03	HAZ

The observation regarding the fractures of the Ti-6Al-4V tensile samples draws attention to the fact that fractures occur at the HAZ for T1-T4, T6, and T7 (as shown in Figure 7(c)). However, T5 is fractured at the thermo-mechanically affected zone (TMAZ), indicating that the weld joint is stronger and more resilient than the other zones, including the base metal. While the tensile strengths for T1, T2, T5, and T7 are slightly lower than that of the base metal, T3, T4, and T6 demonstrate high resistance, with an efficiency 102.61 %, 103.97 %, and 103.97 %, respectively. As a result, T4 exhibits an elongation of 10.96%, a Yield strength of 997.52 MPa, and tensile strength 1031.23 MPa, with a high Young modulus value 115.70 GPa, which explains the high microhardness values achieved for an as RFW joint. In the case of the AA2024 alloy, the fracture occurs most often in the center of the weld joint, indicating that the welded zone is less resistant than the base metal (as depicted in Figure 7(d)). Among the samples, A5 demonstrated the best mechanical properties with a tensile strength 460.09 MPa that corresponds to an efficiency 94.60 % and a moderate rigidity illustrated by a Young modulus 68.23 GPa, while the other samples showed relatively low resistance.

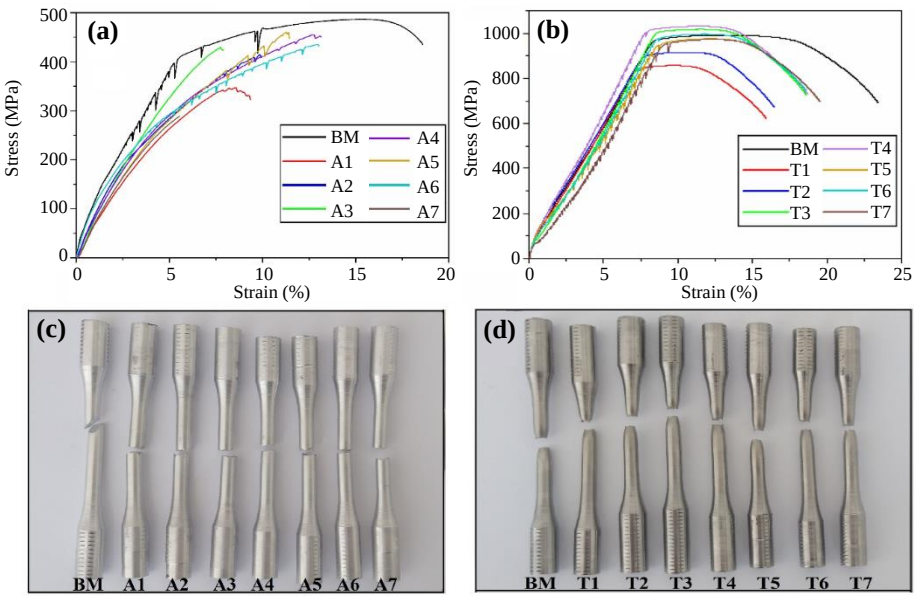

Figure 7 Tensile tests results for (a) AA2024, (b) Ti-6Al-4V, Fractured tensile test samples of (c) AA2024 and (d) Ti-6Al-4V.

Following the cutting of the RFW joints in a longitudinal direction, microhardness measurements were conducted, and nearly symmetrical microhardness profiles were observed for most Ti-6Al-4V samples, with a peak at the interface (Figure 8(a)). Similarly, significant variations were observed in the profiles of each sample in different zones of the AA2024 (Figure 8(b)). These findings are consistent with previous research on Ti-6Al-4V alloy [8, 9] and the AA2024 [30]. T4 and A7 samples of the Ti-6Al-4V and the AA2024 alloys respectively recorded the highest microhardness values. In T4, the microhardness value in the as weld joint was 382 HV in the base metal, with values rising to 511 HV in the DRZ, and reducing to 384 HV and 424 HV in TMAZ and HAZ, respectively, which are comparable to the base metal. A7 in the AA2024 alloy exhibited the best microhardness profile, with a maximum value of 148 HV at the weld interface and an average value 121 HV along HAZ and TMAZ, which is slightly less than the base metal (125 HV).

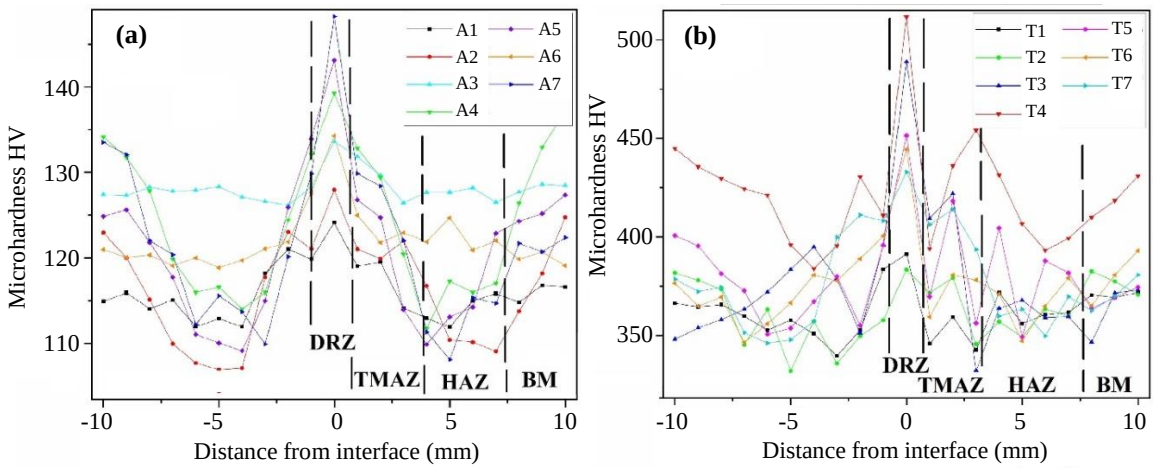

Figure 8 Microhardness measurements for (a) AA2024 and (b) Ti-6Al-4V.

3.2 Microscopic observations

Figure 9 depicts an image of β grains at the interface of T4 sample that were enlarged due to the heat input generated by friction in the DRZ. The α phase appeared as lamellae within the β grains. A discontinuous crack was observed at the weld interface between the two welded parts, which could be attributed to the high normal pressure that extracted most of the pasty material in the form of flash during the RFW process. As a result, there was a lack of material cohesion at the weld interface. Furthermore, the grains were observed to be refined in the TMAZ and HAZ. Figure 10 shows the microstructures of each zone of the AA2024 RFW joint (A5). The intense plastic deformation caused the grains to be refined in the DRZ, while the TMAZ grains changed their orientation according to the material flow direction. The HAZ underwent thermal cycle that led to the dissolution of the precipitates. However, the BM consisted of a set of fine precipitates dispersed in a monophasic solution α. During the RFW process, the heat input generated coupled with the high mechanical stress caused the inter-diffusion phenomenon of atoms at the weld interface. It is important to note that the main bonding mechanism in the friction welding process is diffusion bonding, as reported in previous studies. Additionally, the material mixing plays a crucial role during the friction welding process

The SEM images of the fracture surface for the A5 sample are shown in Figure 11. The central zone of the fracture surface exhibits a mixture of morphologies, as depicted in Figure 11(a), with a large rough part consisting of small cupules, as shown in Figures 11(b)-(c). Additionally, there are relatively smooth and flat areas in the peripheral zone, surrounded by the majority of the cupular surface. The presence of these flat zones indicates inadequate material mixing and insufficient dynamic recrystallization of the grains in the interfacial zone between the two welded parts, leading to low tensile strength. The fracture surface of the T4 sample, as shown in Figures 12(a)-(c), is consistent with the results of Vikas et al. [9]. The morphology is uniform across the entire surface, with material tearing occurring in the form of dimples of various sizes, indicating a ductile fracture mode.

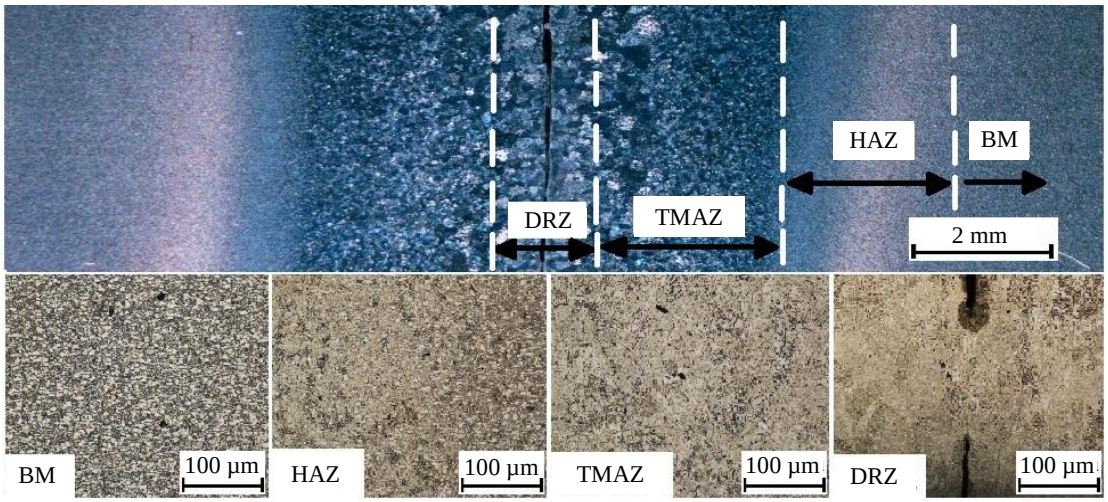

Figure 9 Microstructure of T4 sample.

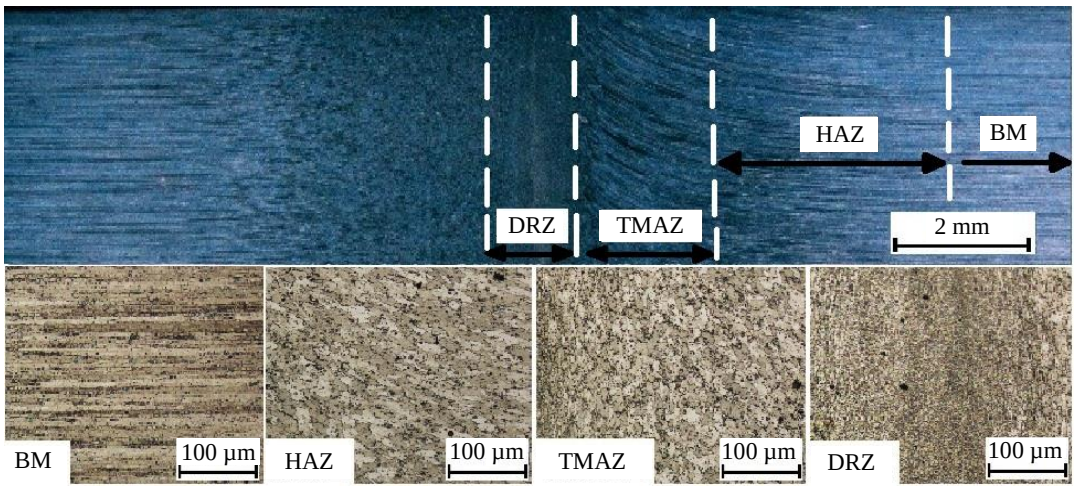

Figure 10 Microstructure of A5 sample.

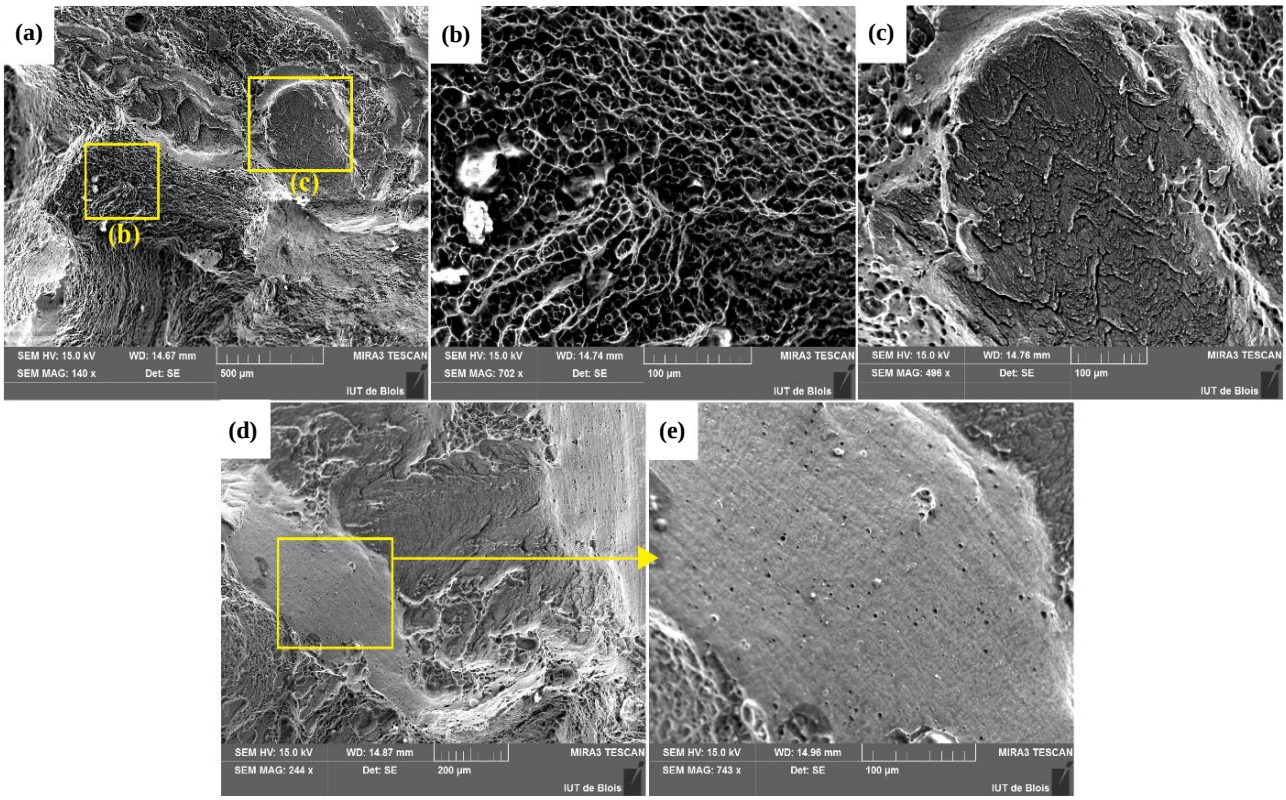

Figure 11 SEM observations of the fracture surface for A5 sample (a, b, and c) Central zone and (d and e) Peripheral zone.

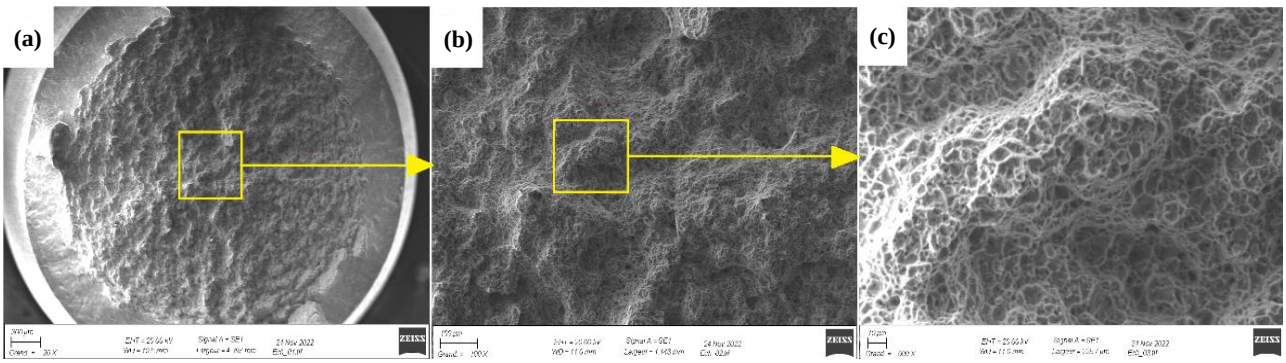

Figure 12 (a) SEM general observations of the fracture surface for T4 sample, (b) Morphology of the fracture surface, (c) Magnification of the boxed zone in (b).

4. Conclusion

An automated RFW system was employed to perform friction welding of AA2024 and Ti-6Al-4V alloys, and their mechanical properties and microstructure were studied to determine the optimal normal pressure. The following conclusions were made:

1. This study demonstrates the feasibility of applying the RFW process by making an instrumented system that automatically controls RFW parameters to perform welding operations.
2. The tensile strength of Ti-6Al-4V RFW joints increased dramatically to 1031.23 MPa, with a joint efficiency of 103.97%, for the weld joint obtained at 8 MPa normal pressure. However, the tensile strength of AA2024 welds was lower than that of the base metal. The best tensile properties for AA2024 were obtained with 10 MPa normal pressure.
3. Almost all Ti-6Al-4V tensile samples fractured through the HAZ, indicating that the weld joint is more resilient than other zones, including the base metal. For AA2024, the fracture typically occurs at the weld interface.
4. The highest microhardness values at the weld interface were observed in RFW joints obtained at 8 MPa and 14 MPa normal pressures for Ti-6Al-4V and AA2024, respectively.
5. Microscopic examination of the fracture surfaces of AA2024 showed a mixture of morphologies, with a dominant rough cupular surface, indicating a ductile fracture mode. For Ti-6Al-4V, dimples of varying sizes were observed over the entire fracture surface, leading to a ductile fracture mode.

5. References

[1] American Welding Society. Recommended practices for friction welding. An American National Standard ANSI/AWS C6.1-89. Miami: American Welding Society; 2009.
[2] Li W, Vairis A, Preuss M, Ma T. Linear and rotary friction welding review. Int Mater Rev. 2016;61(2):71-100.
[3] Meisnar M, Baker S, Bennett JM, Bernad A, Mostafa A, Resch S, et al. Microstructural characterisation of rotary friction welded AA6082 and Ti-6Al-4V dissimilar joints. Mater Des. 2017;132:188-97.
[4] Dressler U, Biallas G, Mercado UA. Friction stir welding of titanium alloy TiAl6V4 to aluminium alloy AA2024-T3. Mater Sci Eng A. 2009;526(1-2):113-7.
[5] Avinash M, Chaitanya GV, Giri DK, Upadhya S, Muralidhara BK. Microstructure and mechanical behaviuor of rotary friction welded titanium alloys. Int J Mater Metall Eng. 2007;1(11):641-3.
[6] Nu HT, Loc NH, Minh LP. Influence of the rotary friction welding parameters on the microhardness and joint strength of Ti6Al4V alloys. Proc Inst Mech Eng B J Eng Manuf. 2021;235(5):795-805.
[7] Jin F, Rao H, Wang Q, Wen G, Liu P, Liu J, et al. Heat-pattern induced non-uniform radial microstructure and properties of Ti-6Al-4V joint prepared by rotary friction welding. Mater Charact. 2023;195:112536.
[8] Zulu M, Mashinini M. Optimisation of the rotary friction welding process of titanium alloy rods. MATEC Web Conf. 2021;347:1-12.
[9] Vikas KS, Rao KS, Rahul, Reddy GM, Ramana VV. Influence of heat treatments on microstructural and mechanical properties of grade 5 titanium friction welds. Eng Res Express. 2022;4(2):025053.
[10] My Nu HT, Le TT, Minh LP, Loc NH. A study on rotary friction welding of titanium alloy (Ti6Al4V). Adv Mater Sci Eng. 2019;2019:1-10.
[11] Sankar GS, Karthik GM, Mohammad A, Kumar R, Janaki Ram GD. Friction welding of electron beam melted γ-TiAl alloy Ti–48Al–2Cr–2Nb. Trans Indian Inst Met. 2019;72(1):35-46.
[12] Hynes NR, Velu PS. Effect of rotational speed on Ti-6Al-4V-AA 6061 friction welded joints. J Manuf Process. 2018;32:288-97.
[13] Li P, Wang S, Dong H, Wen G, Yu F, Ma Y, et al. Effect of inhomogeneous microstructure evolution on the mechanical properties and corrosion behavior of rotary friction welded AA2024 joints. Mater Charact. 2021;178:111306.
[14] Li P, Wang S, Xia Y, Hao X, Lei Z, Dong H. Inhomogeneous microstructure and mechanical properties of rotary friction welded AA2024 joints. J Mater Res Technol. 2020;9(3):5749-60.
[15] Immarigeon JP, Holt RT, Koul AK, Zhao L, Wallace W, Beddoes JC. Lightweight materials for aircraft applications. Mater Charact. 1995;35(1):41-67.
[16] May A, Belouchrani MA, Taharboucht S, Boudras A. Influence of heat treatment on the fatigue behaviour of two aluminium alloys 2024 and 2024 plated. Procedia Eng. 2010;2(1):1795-804.
[17] May A, Belouchrani MA, Manaa A, Bouteghrine Y. Influence of fatigue damage on the mechanical behaviour of 2024-T3 aluminum alloy. Procedia Eng. 2011;10:798-806.
[18] Zhang L, Liu X, Wang L, Wu S, Fang H. A model of continuum damage mechanics for high cycle fatigue of metallic materials. Trans Nonferrous Met Soc China. 2012;22(11):2777-82.
[19] May A, Taleb L, Belouchrani MA. Analysis of the cyclic behavior and fatigue damage of extruded AA2017 aluminum alloy. Mater Sci Eng A. 2013;571:123-36.
[20] Bois-Brochu A, Blais C, Goma FAT, Larouche D, Boselli J, Brochu M. Characterization of Al–Li 2099 extrusions and the influence of fiber texture on the anisotropy of static mechanical properties. Mater Sci Eng A. 2014;597:62-9.
[21] May A. On the origins of the anisotropic mechanical behaviour of extruded AA2017 aluminium alloy. Bull Mater Sci. 2017;40(2):395-406.
[22] Lakache HE, May A, Badji R. Rotary friction welding parameters effects upon mechanical properties and microstructure of AA2024 weld joints. Eng Sol Mech. In press 2023.
[23] Li X, Li J, Jin F, Xiong J, Zhang F. Effect of rotation speed on friction behavior of rotary friction welding of AA6061-T6 aluminum alloy. Weld World. 2018;62(5):923-30.
[24] Hariprasath P, Sivaraj P, Balasubramanian V. A critical assessment on rotary friction welded high strength armor grade aluminum alloy joints. Phys Metals Metallogr. 2021;122(13):1401-8.
[25] Dang Z, Qin G, Ma H. Interfacial microstructural characterization and mechanical properties of inertia friction welding of 2219 aluminum alloy to 304 stainless steel. Mater Sci Eng A. 2021;822:141689.
[26] Dong H, Yang J, Li Y, Xia Y, Hao X, Li P, et al. Evolution of interface and tensile properties in 5052 aluminum alloy/304 stainless steel rotary friction welded joint after post-weld heat treatment. J Manuf Process. 2020;51:142-50.

[27] Sharma C, Dwivedi DK, Kumar P. Effect of welding parameters on microstructure and mechanical properties of friction stir welded joints of AA7039 aluminum alloy. Mater Des (1980-2015). 2012;36:379-90.
[28] Trimble D, O'Donnell GE, Monaghan J. Characterisation of tool shape and rotational speed for increased speed during friction stir welding of AA2024-T3. J Manuf process. 2015;17:141-50.
[29] Sundaram NS, Murugan N. Dependence of ultimate tensile strength of friction stir welded AA2024-T6 aluminium alloy on friction stir welding process parameters. Mechanika. 2009;78(4):17-24.
[30] Mimouni O, Badji R, Kouadri-David A, Gassaa R, Chekroun N, Hadji M. Microstructure and mechanical behavior of friction-stir-welded 2017A-T451 aluminum alloy. Trans Indian Inst Met. 2019;72(7):1853-68.
[31] International Organization for Standardization. EN ISO 6892-1:2016 - Metallic materials - Tensile testing – Part 1: Method of test at room temperature. Brussels: European Committee for Standardization; 2016.
[32] Combres Y, Champin B. Recent developments of the titanium industry and research in France. In: Blenkinsop PA, Evans WJ, Flower HM, editors. Titanium '95: Science and Technology; 1995 Oct 22-26; Birmingham, United Kingdom. London: Institute of Materials; 1996. p. 11-20.
[33] Al-Rubaie KS, Melotti S, Rabelo A, Paiva JM, Elbestawi MA, Veldhuis SC. Machinability of SLM-produced Ti6Al4V titanium alloy parts. J Manuf Process. 2020;57:768-86.
[34] Castro R, Seraphin L. Contribution à l'étude métallographique et structurale de l'alliage de titane ta6v. Mem Sci Rev Met. 1966; 63:1025-58. (In French)
[35] Murugan SS, Sathiya P, Haq AN. Continuous drive dissimilar friction welding of wrought aluminium AA6063-T6 and austenitic stainless steel AISI304L with different welding methods and welding trials. Kovove Mater Metal Mater. 2021;59(3):161-9.
[36] Kimura M, Choji M, Kusaka M, Seo K, Fuji A. Effect of friction welding conditions and aging treatment on mechanical properties of A7075-T6 aluminium alloy friction joints. Sci Technol Weld Join. 2005;10(4):406-12.
[37] Wang GL, Li JL, Wang WL, Xiong JT, Zhang FS. Rotary friction welding on dissimilar metals of aluminum and brass by using pre-heating method. Int J Adv Manuf Technol. 2018;99(5):1293-300.
[38] Vairis A, Papazafeiropoulos G, Tsainis AM. A comparison between friction stir welding, linear friction welding and rotary friction welding. Adv Manuf. 2016;4(4):296-304.